

Article

Branched Electron-Donor Core Effect in D- π -A Star-Shaped Small Molecules on Their Properties and Performance in Single-Component and Bulk-Heterojunction Organic Solar Cells †

Alexander N. Solodukhin ^{1,‡}, Yuriy N. Luponosov ^{1,*,‡}, Artur L. Mannanov ^{1,2}, Petr S. Savchenko ¹, Artem V. Bakirov ^{1,3}, Maxim A. Shcherbina ^{1,4}, Sergei N. Chvalun ^{1,3}, Dmitry Yu. Paraschuk ^{1,2,*} and Sergey A. Ponomarenko ¹

- ¹ Enikolopov Institute of Synthetic Polymeric Materials of the Russian Academy of Sciences, Profsoyuznaya St. 70, 117393 Moscow, Russia; solodukhin@ispm.ru (A.N.S.); al.mannanov@physics.msu.ru (A.L.M.); muncake101@gmail.com (P.S.S.); bakirov.artem@gmail.com (A.V.B.); max-shcherbina@yandex.ru (M.A.S.); s-chvalun@yandex.ru (S.N.C.); ponomarenko@ispm.ru (S.A.P.)
- ² Faculty of Physics, Lomonosov Moscow State University, Leninskie Gory 1/62, 119991 Moscow, Russia
- ³ National Research Centre Kurchatov Institute, 1 ak. Kurchatov Square, 123098 Moscow, Russia
- ⁴ Moscow Institute of Physics and Technology, 9 Institutsky Line, Dolgoprudny, 141700 Moscow, Russia
- * Correspondence: luponosov@ispm.ru (Y.N.L.); paras@physics.msu.ru (D.Y.P.)
- † This paper is an extended version of our conference abstracts published in 2020 Online School on Hybrid, Organic and Perovskite Photovoltaics (HOPE-PV20) 3–5 November 2020; p. 24.
- ‡ Alexander N. Solodukhin and Yuriy N. Luponosov contributed equally to this work.



Citation: Solodukhin, A.N.; Luponosov, Y.N.; Mannanov, A.L.; Savchenko, P.S.; Bakirov, A.V.; Shcherbina, M.A.; Chvalun, S.N.; Paraschuk, D.Y.; Ponomarenko, S.A. Branched Electron-Donor Core Effect in D- π -A Star-Shaped Small Molecules on Their Properties and Performance in Single-Component and Bulk-Heterojunction Organic Solar Cells. *Energies* **2021**, *14*, 3596. <https://doi.org/10.3390/en14123596>

Academic Editor: Emmanuel Kymakis

Received: 19 May 2021

Accepted: 9 June 2021

Published: 17 June 2021

Publisher's Note: MDPI stays neutral with regard to jurisdictional claims in published maps and institutional affiliations.



Copyright: © 2021 by the authors. Licensee MDPI, Basel, Switzerland. This article is an open access article distributed under the terms and conditions of the Creative Commons Attribution (CC BY) license (<https://creativecommons.org/licenses/by/4.0/>).

Abstract: Star-shaped donor-acceptor molecules are full of promise for organic photovoltaics and electronics. However, the effect of the branching core on physicochemical properties, charge transport and photovoltaic performance of such donor-acceptor materials in single-component (SC) and bulk heterojunction (BHJ) organic solar cells has not been thoroughly addressed. This work shows the comprehensive investigation of six star-shaped donor-acceptor molecules with terminal hexyldicyanovinyl blocks linked through 2,2'-bithiophene π -conjugated bridge to different electron-donating cores such as the pristine and fused triphenylamine, *tris*(2-methoxyphenyl)amine, carbazole and benzotriindole-based units. Variation of the branching core strongly impacts on such important properties as the solubility, highest occupied molecular orbital energy, optical absorption, phase behavior, molecular packing and also on the charge-carrier mobility. The performance of SC or BHJ organic solar cells are comprehensively studied and compared. The results obtained provide insight on how to predict and fine-tune photovoltaic performance as well as properties of donor-acceptor star-shaped molecules for organic solar cells.

Keywords: donor-acceptor small molecules; star-shaped molecules; triphenylamine; carbazole; benzotriindole; single-component organic solar cells; bulk-heterojunction organic solar cells

1. Introduction

Organic solar cells are attracting considerable attention due to their ability to produce flexible, lightweight devices with solvent and printing technologies [1–6]. Power conversion efficiency (PCE) has exceeded 16% over the last few years [7–9]. In the design of small molecules, the donor–acceptor (D–A) concept is the most successful one for organic photovoltaics and other optoelectronic applications. In general, the concept includes variation of types and numbers of electron-donor and electron-withdrawing groups or their sequence within the molecular structure, which results in a lower bandgap by reason of orbital mixing of the donor and the acceptor blocks and shifts absorption into the long-wave region due to the intramolecular charge transfer (ICT) effects [10–13]. Investigations of D–A small molecules demonstrate that even minor adjustments in the molecule structure can lead

to significant changes in material characteristics, which may be used for fine tuning the material properties [14–16]. Donor-acceptor molecules of star-shaped architecture have several advantages over linear ones, for example, enhanced solubility, lower anisotropy of electrical and optical properties, higher value of molar extinction coefficients and increased number of pathways for light conversion [17–25]. Triphenylamine (TPA) is a branching core widely used to design hole-transporting star-shaped and branched molecules for various optoelectronic applications [22,23,26–32]. The propeller-shaped form of TPA inhibits strong π - π interactions between neighboring groups and because of that the great number of TPA derivatives are amorphous and soluble. Benefits of amorphous materials include absence of the necessity to carry out a posttreatment of functional layers in optoelectronic devices and formation of homogeneous contacts at interfaces of organic-metal or organic-organic layers. However, it is well-known that amorphous materials, when compared to crystalline organic semiconductors, demonstrate much less efficient charge transport. One of the possible approaches to solve the problem is a chemical modification of the TPA core or usage of other more ridged and planar cores. It was shown that the addition of the methoxy groups into the TPA can increase crystallinity of the target materials [33]. Phenyl-substituted carbazoles can be considered as the nearest but partly fused and more planar analogs of the TPA core [34–37]. The complete covalent fusing of the TPA core is another tool to convert propeller-like TPA to the planar core [38–40]. Benzotriindole (BTI) core [41] being a truxene analogue, but with three nitrogen atoms instead of carbon ones, is one of the promising planar cores to design star-shaped structures of the molecules for organic photonics and photovoltaics [42–45].

Single-component (SC) OSCs, being a separate field of organic photovoltaics, have attracted much attention due to a simple device structure and the lack of time-dependent active layer phase segregation [46–48]. SC OSCs are showing rapid advances and the most efficient devices based on so-called “double-cable” polymers are now approaching over 8% PCE [49]. In fact, the “double-cable” polymers or similar small molecule dyads consist of donor and acceptor units linked to each other through an aliphatic spacer within one molecule. The drawbacks of these concepts are a relatively complex synthesis and the necessity to carry out a posttreatment of functional layers in the devices to tune the miscibility between conjugated backbones and side units. In contrast to them, simple conjugated small molecules and polymers do not suffer from that and demonstrate high open circuit voltage (V_{OC}) in SC OSCs [50,51]. The PCE of SC OSCs based on such materials have recently reached a remarkable 2.9% [52]. However, the library of appropriate small molecules for this purpose is scarce and many aspects, such as the correlation between the structure, properties and performance in SC devices, remain poorly addressed, which limits the further boost of the PCE for SC OSCs. Therefore, the development and comprehensive investigation of novel conjugated small molecules for SC OSCs are urgently needed.

In our recent reports we have demonstrated that TPA-based donor-acceptor star-shaped molecules have a field-assisted mechanism of charge photogeneration and demonstrate small energy losses resulting in high open-circuit voltage up to 1.19 V and the power conversion efficiency over 1% [53–55]. However, a detailed investigation of the impact of core type on the performance of donor-acceptor star-shaped molecules in SC OSCs has never been conducted.

This work reports on the comprehensive investigation of six star-shaped D-A molecules having electron-withdrawing terminal hexyldicyanovinyl fragments linked through the 2,2'-bithiophene π -spacer to the different branching cores: triphenylamine (TPA) [56], tris(2-methoxyphenyl)amine (**m-TPA**), 4,4,8,8,12,12-hexakis(4-methylphenyl)-4*H*,8*H*,12*H*-benzo[1,9]quinolizino[3,4,5,6,7-*defg*]acridine (**f-TPA**), 9-phenyl-9*H*-carbazole (**s-CBZ**), 2,7-dibromo-9-(4-bromophenyl)-9*H*-carbazole (**t-CBZ**) [35] or 5,10,15-triethyl-10,15-dihydro-5*H*-diindolo[3,2-*a*:3',2'-*c*]carbazole (**BTI**) [57] (Figure 1). The comparison of their properties and photovoltaic devices performance allows the impact of the donor branching core type on the solubility, phase behavior, optical, electrochemical properties and photoelectric characteristics of SC and BHJ OSCs to be revealed.

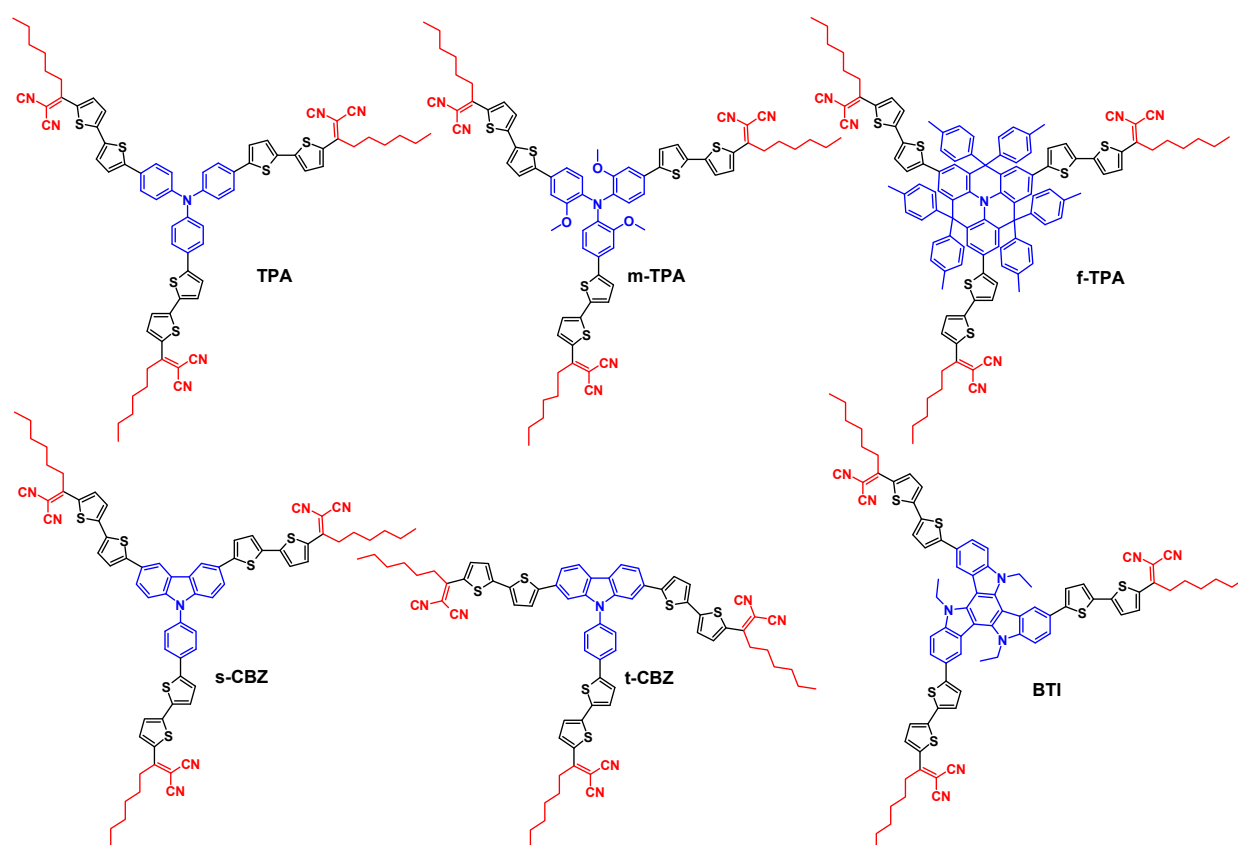


Figure 1. Chemical structures of the star-shaped donor-acceptor molecules: TPA, m-TPA, f-TPA, s-CBZ, t-CBZ and BTI.

2. Results and Discussion

2.1. Synthesis

The synthesis of **m-TPA** and **f-TPA** molecules was carried out according to the previously developed scheme for the preparation of similar star-shaped compounds (Figure 2) [58,59].

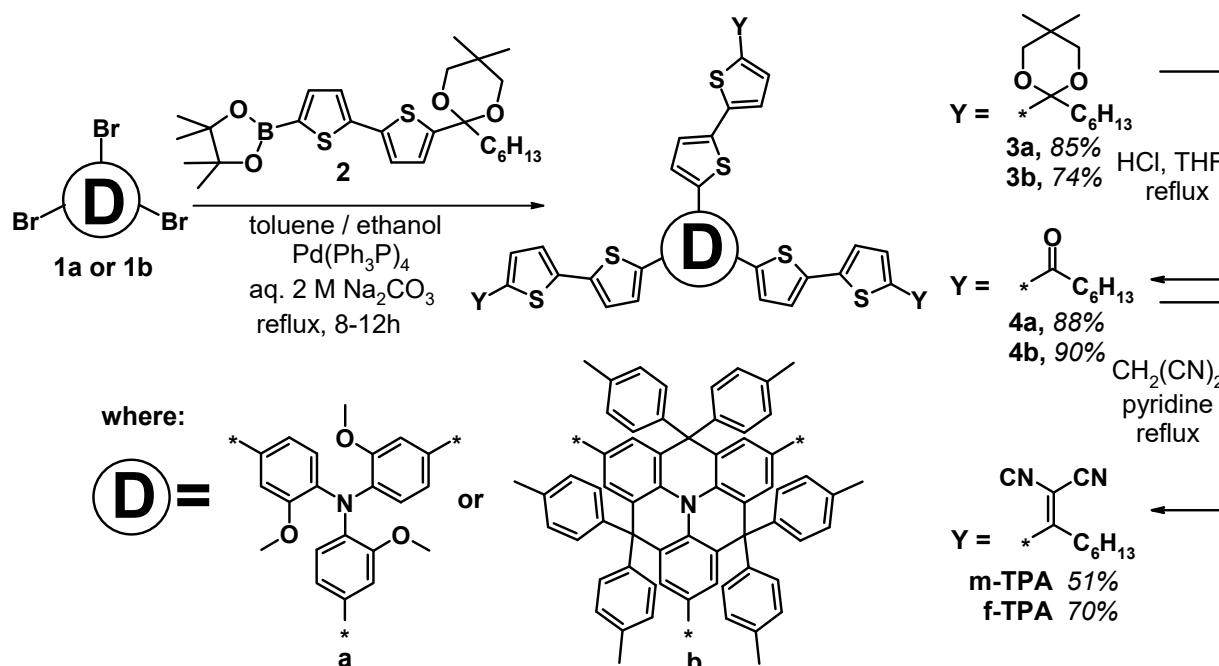


Figure 2. Scheme synthesis of **m-TPA** and **f-TPA** molecules.

First, star-shaped ketals, namely, *tris*{4-[5'-(2-hexyl-5,5-dimethyl-1,3-dioxan-2-yl)-2,2'-bithien-5-yl]-2-methoxyphenyl}amine (**3a**) and 2,6,10-*tris*{5'-(2-hexyl-5,5-dimethyl-1,3-dioxan-2-yl)-2,2'-bithien-5-yl}-4,4,8,8,12,12-hexakis(4-methylphenyl)-4*H*,8*H*,12*H*-benzo[1,9]quinolizino[3,4,5,6,7-*defg*]acridine (**3b**) were synthesized. Compounds **3a** and **3b** were obtained by Suzuki cross-coupling between *tris*(4-bromo-2-methoxyphenyl)amine (**1a**) or 2,6,10-tribromo-4,4,8,8,12,12-hexakis(4-methylphenyl)-4*H*,8*H*,12*H*-benzo[1,9]quinolizino[3,4,5,6,7-*defg*]acridine (**1b**) and 2-hexyl-5,5-dimethyl-2-[5'-(4,4,5,5-tetramethyl-1,3,2-dioxaborolan-2-yl)-2,2'-bithien-5-yl]-1,3-dioxane [59] (**2**) in 85% and 74% yields, respectively. Second, the star-shaped ketones 1,1',1''-[nitriolo*tris*[(3-methoxy-4,1-phenylene)-2,2'-bithiene-5',5'-diyl]]trihexan-1-one (**4a**) and 1,1',1''-[[4,4,8,8,12,12-hexakis(4-methylphenyl)-4*H*,8*H*,12*H*-benzo[1,9]quinolizino[3,4,5,6,7-*defg*]acridine-2,6,10-triyl]*tris*(2,2'-bithiene-5',5'-diyl)]trihexan-1-one (**4b**) were obtained by refluxing of the ketals **3a** and **3b** in THF solution with 1M HCl in 88% and 90% yields, respectively. Finally, *tris*{4-[5'-(1,1-dicyanooct-1-en-2-yl)-2,2'-bithien-5-yl]-2-methoxyphenyl}amine (**m-TPA**) and 2,2',2''-[[4,4,8,8,12,12-hexakis(4-methylphenyl)-4*H*,8*H*,12*H*-benzo[1,9]quinolizino[3,4,5,6,7-*defg*]acridine-2,6,10-triyl]*tris*(2,2'-bithiene-5',5'-diyl)hept-1-yl-1-ylidene]]trimalononitrile (**f-TPA**) were obtained by Knoevenagel condensation of the ketones **4a** or **4b** with malononitrile in 51% and 70% yields, respectively. The chemical structure and high purity of the target products were confirmed by a complex of methods (see Experimental Part in Electronic Supplementary Information (ESI), Figures S2.1–S2.11).

2.2. Solubility, Thermal and Structural Properties

Thermal and thermo-oxidative stability were investigated by thermogravimetric analysis (TGA) and the data are summarized in Figure 3 and Table 1. The materials showed a high thermal-oxidative stability with the decomposition temperature (T_d) exceeding 360 °C (Figure 3a, Table 1) and no clear dependence of the T_d from the branching core type. Considering the thermal stability in the inert atmosphere (Figure 3b), one can see that the **m-TPA** and **BTI** compounds that have the thermally less stable aliphatic substituents at the core show the lowest T_d within the series of molecules. In contrast, **f-TPA** shows the highest T_d since it has phenyl substituents at the core.

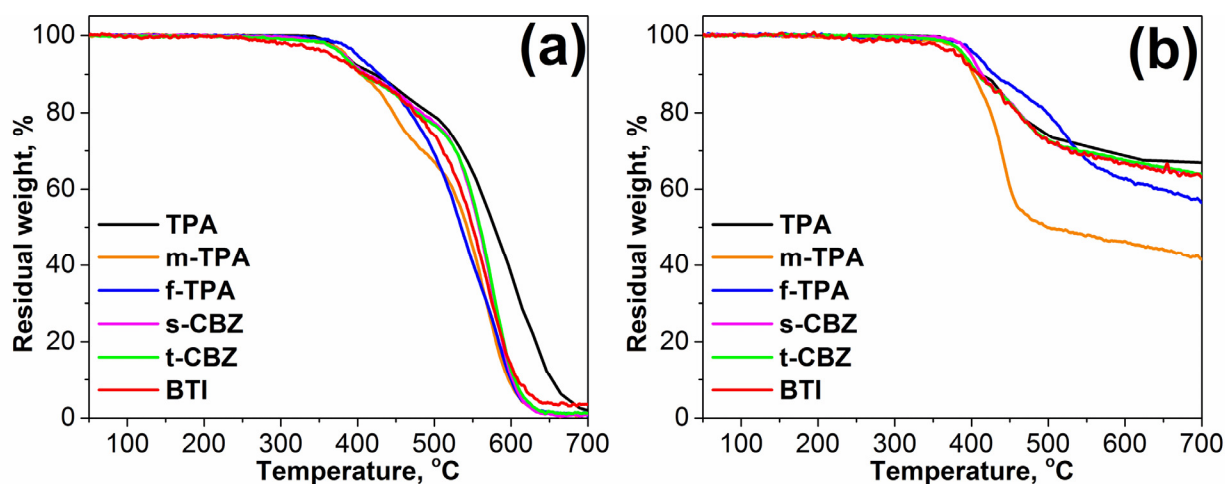


Figure 3. TGA curves of TPA, m-TPA, f-TPA, s-CBZ, t-CBZ and BTI in air (a) and under inert atmosphere (b).

The phase behavior of the materials was studied by differential scanning calorimetry (DSC). The results are summarized in Figure 4 and Table 1. According to the DSC scans of the first heating (see Figure 4a) and X-Ray diffraction data (see below) most of the molecules as received are amorphous. Molecules based on rather similar triphenylamine and carbazole cores with no substituents (**TPA**, **s-CBZ** and **t-CBZ**) showed alike glass transition temperatures (T_g) at the 64–66 °C region. However, it should be noted that **t-CBZ** with T-like molecular geometry is able to crystallize above T_g . Modification of the

TPA core by introduction of the methoxy substituents leads to the slight increase in T_g up to 71 °C due to enhanced intermolecular interactions [59,60]. Comparing **TPA** and **f-TPA** one can see that the latter's T_g is more than twice that of the former's (64 °C vs. 137 °C), which can be explained by a higher molecular weight and an increased molecular rigidity of the fused molecule. An important difference in the phase behavior of **f-TPA** is the ability to crystallize above T_g followed by melting at 300 °C with an enthalpy (ΔH_m) of 34 Jg⁻¹. The phase behavior of the planar **BTI** is like that of **f-TPA** but does not show any glass transition and melts at 231 °C with ΔH_m of 42 Jg⁻¹. It is interesting to note that among this series of molecules the **t-CBZ** and **BTI** molecules retain the ability to crystallize from the melt as well, whereas crystallization of the other materials is hindered, and they show only a glass transition on DSC scans at the subsequent heating (Figure 4b).

Table 1. Solubility, thermal data and phase behavior of oligomers.

Compounds	Solubility ^a , gL ⁻¹	T_g , °C	ΔC_p , J(gK) ⁻¹	T_{m1} , °C	ΔH_{m1} , Jg ⁻¹	T_{m2} , °C	ΔH_{m2} , Jg ⁻¹	T_d (Air/N ₂), °C
TPA	20	64	0.3	–	–	–	–	383/390
m-TPA	43	71	0.3	–	–	–	–	384/389
f-TPA	49	137	0.2	300	34	–	–	400/406
s-CBZ	24	66	0.4	–	–	–	–	379/397
t-CBZ	30	64	0.2	120	7	120	5	379/389
BTI	5	–	–	231	42	223	24	365/380

Notes: ^a measured in ODCB; T_g —glass transition temperature; ΔC_p —jump of heat capacity at T_g ; T_{m1} and T_{m2} are the melting temperature according to the first and second DSC scans, respectively; ΔH_{m1} and ΔH_{m2} —melting enthalpy according first and second DSC scans, respectively; T_d —decomposition temperature corresponding to 5% of the weight loss.

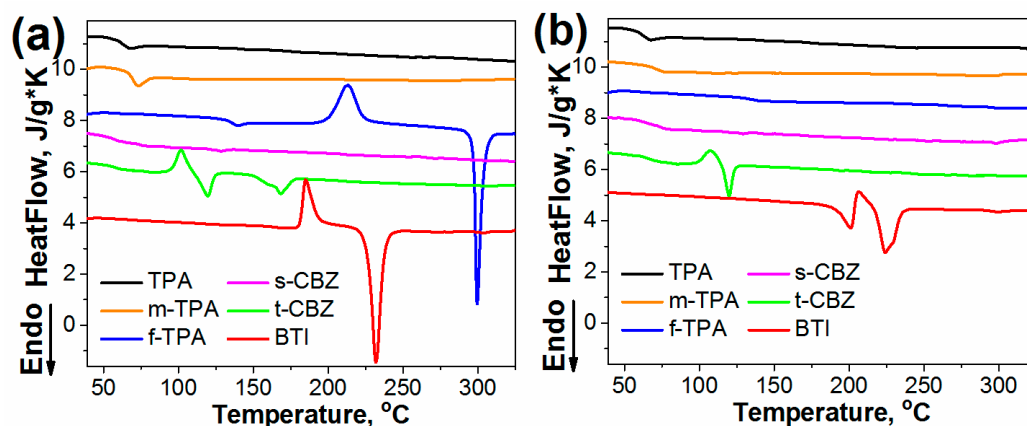


Figure 4. DSC first (a) and second (b) heating scans of **TPA**, **m-TPA**, **f-TPA**, **s-CBZ**, **t-CBZ** and **BTI**.

The solubility of the molecules was measured in *o*-dichlorobenzene (ODCB) solutions (Table 1). The solubility of the **s-CBZ** and **t-CBZ** molecules that have carbazole cores is slightly higher as compared to that of **TPA** molecule. The presence of the both methoxy and bulky *p*-tolylmethene substituents at the TPA core leads to a more than twice increase in solubility of **m-TPA** and **f-TPA** molecules as compared to the pristine **TPA**. The **BTI** compound, having the completely planar core, showed the lowest and quite modest solubility.

X-ray structural data (Figure 5a) are in a good agreement with the DSC data. X-ray diffraction patterns of all but **t-CBZ** compounds reveal only a broad halo corresponding to the amorphous state of the matter. Crystalline structure of **t-CBZ** was described in detail in our earlier work [35]. However, after annealing, the **f-TPA** and **BTI** samples become highly crystalline, each manifesting tens of narrow reflections, their halfwidths corresponding to the crystallite sizes higher than 30 nm. Such separation can be easily understood, as in all crystalline compounds the core is flat and end-to-end conjugated providing good possibilities for tight packing of the molecules in the crystal lattice. On the

other hand, cores of molecules of the amorphous compounds are substantially warped, having a fan-type shape.

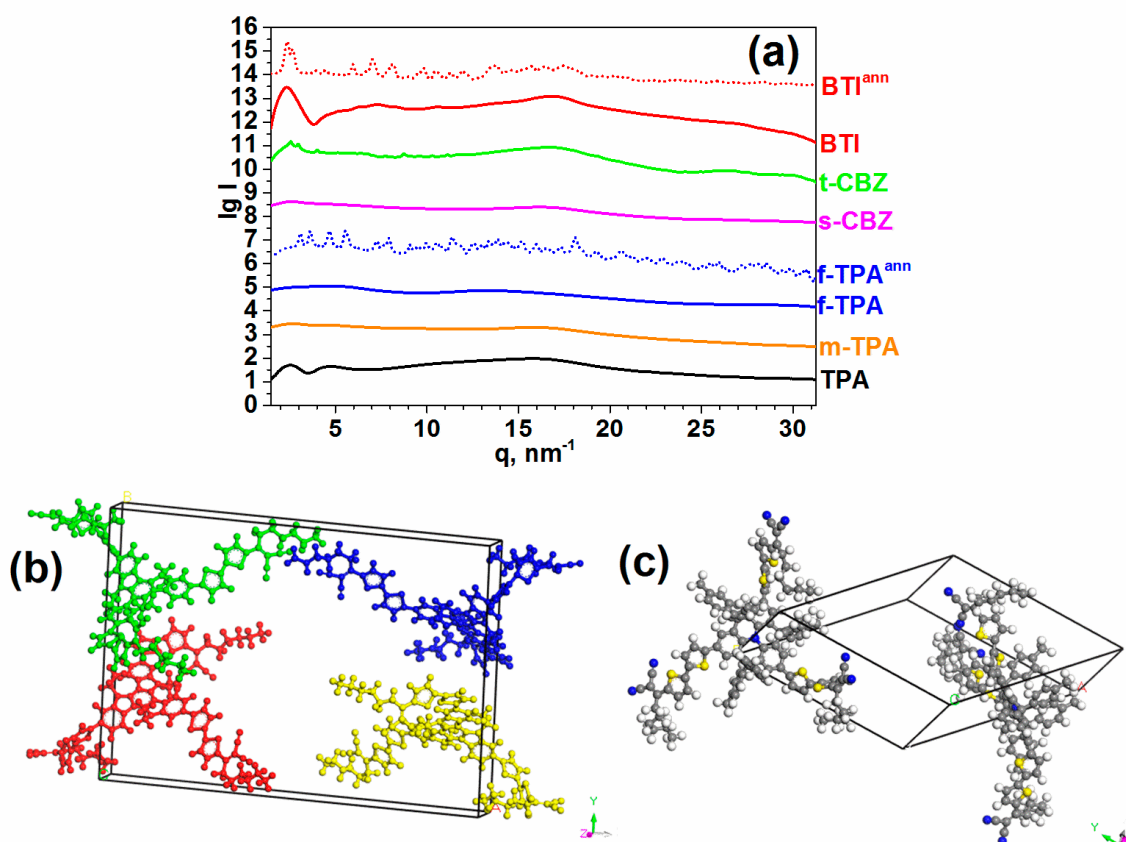


Figure 5. (a) XRD patterns of as-received (solid lines) and annealed (dotted lines) samples of the studied compounds. For the sake of clarity experimental curves are shifted along the intensity axis. Molecular modelling of crystal cell packing solutions for **BTI** (b) and **f-TPA** (c).

Indexing of the provided X-ray data for three crystalline compounds was carried out using *Accelrys Material Studio* program (Table 2 and Figure 5). As expected, in all three cases, the crystallization is induced by the wide planar contact of the conjugated parts of the molecules. Such packing is the necessary condition for intermolecular electron transfer.

Table 2. Crystal cell parameters of **t-CBZ**, **f-TPA** and **BTI**.

Sample	System	<i>a</i> , Å	<i>b</i> , Å	<i>c</i> , Å	α°	β°	γ°	<i>V</i> , Å ³
t-CBZ	Monoclinic	18.5	24.5	9.4	90	95.7	90	4240
f-TPA	Triclinic	25.9	21.6	11.1	93.7	91.9	129	4780
BTI	Orthorhombic	46.1	31.7	4.3	90	90	90	6299

2.3. Optical and Electrochemical Properties

The optical properties of the molecules in diluted THF solutions and thin films were studied by UV-vis absorption spectroscopy and the data are summarized in Figure 6 and Table 3. In the solutions, all the compounds showed quite similar absorption spectra shape: the bands at the high-energy region (300–420) nm are usually ascribed to π - π^* transitions, whereas the intensive bands at 490–550 nm are ascribed to the ICT [17,61] or to a mixed character [62]. Among this series of molecules, **s-CBZ** and **t-CBZ** have the most blue-shifted absorption spectra. In contrast, **m-TPA** and **f-TPA** with the modified TPA core have the most red-shifted absorption spectra. The absorption maxima (λ_{\max}) of **BTI** and **TPA** were found to be red-shifted as compared to **s-CBZ** and **t-CBZ** and blue-shifted

as compared to **m-TPA** and **f-TPA** (Figure 6, Table 3). These facts can be explained by the narrowing of the bandgap as confirmed by cyclic voltammetry (CV) data (see below). The absorption spectra of films are significantly shifted to the long-wavelength region and broadened for all materials in comparison with the spectra of solutions (Figure 6b). The most pronounced shift was found to be for the **BTI** molecule, which has the planar core and thus an increased ability to aggregate.

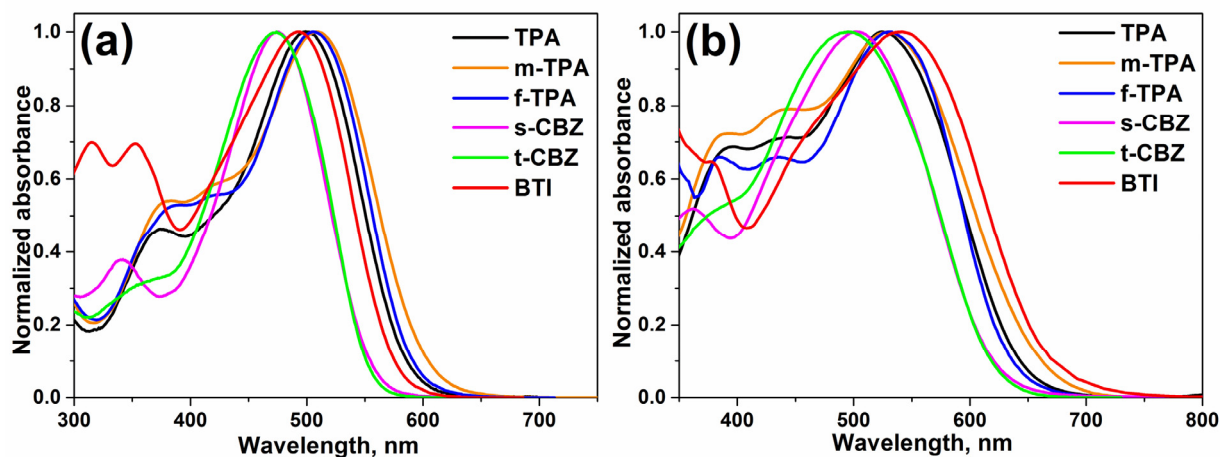


Figure 6. UV-vis absorption spectra of oligomers in THF solutions (a) and films cast from THF (b).

Table 3. Optical and electrochemical data of oligomers.

Compound	λ_{\max}^a , nm	λ_{\max}^b , nm	λ_{onset}^c , nm	E_g^{opt} , eV	HOMO ^d , eV	LUMO ^d , eV	E_g^d , eV
TPA	500	525	637	1.95	−5.34	−3.41	1.93
m-TPA	509	529	662	1.87	−5.20	−3.39	1.81
f-TPA	506	533	636	1.95	−5.30	−3.38	1.92
s-CBZ	475	502	620	2.00	−5.45	−3.35	2.10
t-CBZ	476	496	618	2.01	−5.44	−3.34	2.10
BTI	493	542	663	1.87	−5.36	−3.32	2.04

Notes: ^a Measured in THF solution. ^b Films cast from THF solution. ^c Determined as an intersection between the tangent to the film's absorption edge and the abscissa axis. ^d Calculated from CV experiments.

The highest occupied molecular orbital (HOMO) and lowest unoccupied molecular orbital (LUMO) energies were calculated from oxidation and reduction potentials (see SI). All the molecules have close LUMO energies (Table 3), since the reduction proceeds mainly at the hexyldicyanovinyl electron-withdrawing groups which are the same for all the compounds. In contrast, the type of branching core has a pronounced impact on the HOMO energies. The HOMO energies were found to range from −5.45 eV to −5.20 eV, indicating an increase in the core electron-donating ability in the following sequence: **s-CBZ**–**t-CBZ**–**BTI**–**TPA**–**f-TPA**–**m-TPA**. As a result, the electrochemical bandgap of the molecules can be tuned from 1.93 to 2.04 eV, which agrees well with the optical absorption data.

2.4. Charge Transport and Photovoltaic Properties

2.4.1. Single-Component Solar Cells

The active layer of SC OSC should have comparable hole and electron mobilities to ensure efficient charge transport to electrodes after exciton dissociation. The hole and electron mobilities in films measured by space charge limited current (SCLC) technique (for details see Supplementary Materials) are presented in Table 4 (*J-V* characteristics of the hole and electron only devices are presented in Figures S3.1–3.12).

Table 4. Hole (μ_h) and electron (μ_e) mobilities in pristine films.

Material	$\mu_h, \text{cm}^2/\text{Vs}$	$\mu_e, \text{cm}^2/\text{Vs}$	μ_h/μ_e
TPA	$(1.5 \pm 0.4) \cdot 10^{-4}$	$(1.15 \pm 0.12) \cdot 10^{-5}$	13.0
m-TPA	$(1.36 \pm 0.15) \cdot 10^{-4}$	$(1.24 \pm 0.20) \cdot 10^{-5}$	11.0
f-TPA	$(7.7 \pm 1.3) \cdot 10^{-5}$	$(5.8 \pm 1.3) \cdot 10^{-6}$	13.3
s-CBZ	$(4.8 \pm 1.0) \cdot 10^{-5}$	$(3.8 \pm 0.7) \cdot 10^{-6}$	12.6
t-CBZ	$(3.4 \pm 0.9) \cdot 10^{-5}$	$(4.2 \pm 0.8) \cdot 10^{-6}$	8.1
BTI	$(2.6 \pm 0.7) \cdot 10^{-4}$	$(8.3 \pm 1.6) \cdot 10^{-6}$	31.3

The balanced transport of holes and electrons should be beneficial for SC OSC to avoid space charge effects. At the same time charge carrier mobilities that are too low can increase recombination losses, which reduce the device performance. All investigated compounds showed ambipolar charge transport with almost the same ratio $\mu_h/\mu_e \sim 10$ (Table 4), with the exception of **BTI** for which this ratio is three times greater. **TPA**, **m-TPA** and **BTI** showed the highest values of hole and electron mobilities, so we can expect the best performance of SC OSCs based on them.

The main photovoltaic properties of SC OSCs are presented in Figure 7 and summarized in Table 5 (averaged photovoltaic parameters are presented in SI, Table S1). For the OSCs based on **f-TPA**, **t-CBZ** and **BTI**, which are able to crystallize according to the DSC data (Figure 4), thermal annealing for ordering of the active layer was applied. In the case of **f-TPA** and **t-CBZ**, thermal annealing did not result in an increased PCE due to decreased V_{OC} . However, SC OSC based on **BTI** showed 24% higher efficiency due to increased J_{SC} and FF.

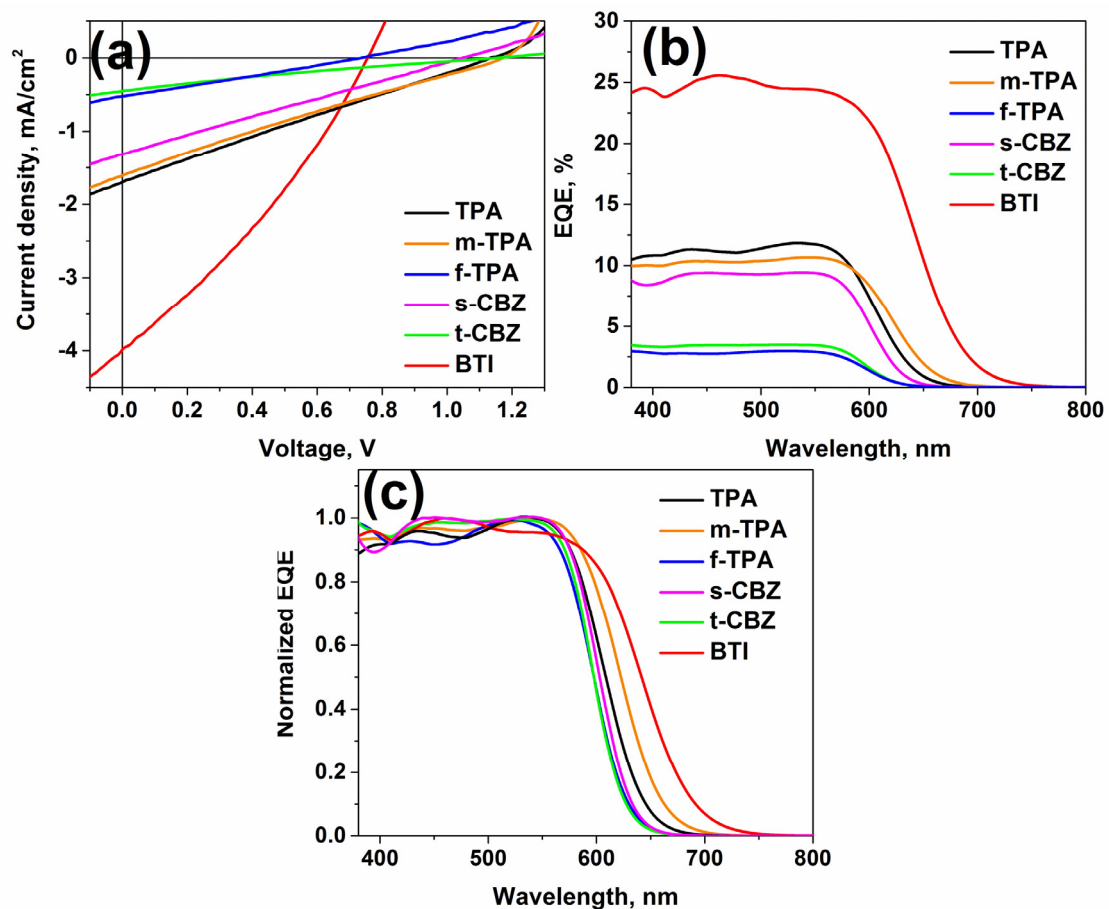


Figure 7. J - V curves under AM1.5G illumination ($100 \text{ mW}/\text{cm}^2$) (a), EQE spectra (b) and normalized EQE spectra (c) for SC OSCs.

Table 5. The best photovoltaic parameters of SC OSCs under AM1.5G illumination (100 mW/cm²) and maximum EQE values.

Active Layer Material	J_{SC} , mA/cm ²	$J_{SC\ EQE}^a$, mA/cm ²	V_{OC} , V	FF, %	PCE, %	EQE, %
TPA	1.70	1.55	1.13	24.3	0.47	11.8
m-TPA	1.61	1.52	1.17	23.2	0.44	10.7
f-TPA	0.52	0.37	0.74	25.7	0.10	3.0
s-CBZ	1.31	1.22	1.05	24.6	0.34	9.4
t-CBZ	0.45	0.44	1.15	21.0	0.11	3.5
BTI^b	3.98	3.86	0.76	31.1	0.94	25.6

Note: ^a $J_{SC\ EQE}$ —short-circuit current integrated from the EQE spectrum. ^b Data for the annealed (180 °C) active layer.

The exceptional position of **BTI** in terms of transport and photovoltaic properties is in agreement with the data of atomic force microscopy (AFM) (SI, Figure S3.19). While films based on all other oligomers have smooth surfaces with indistinguishable morphologies and RMS roughness in the range of 0.30–0.37 nm, the **BTI** film has a much higher roughness of 4.60 nm, which confirms its high crystallinity.

As expected from transport properties, **TPA**, **m-TPA** and **BTI** demonstrated higher PCE values in SC OSCs, and the most efficient was **BTI**. SC OSCs differ mainly in J_{SC} , while the values of V_{OC} ~1.1–1.2 V (except for **f-TPA** and **BTI**) and FF ~25% (except for **t-CBZ** and **BTI**) are about the same. Such V_{OC} values are among the highest for SC OSCs [62]. The relatively low V_{OC} value for **BTI** is possibly related to high crystallinity according to AFM data (Figure S3.19f), since in this case the formation of shunts and increased leakage currents are possible. The low V_{OC} value for **f-TPA** can be associated with the presence of bulky PhMe groups surrounding the donor core, which can hinder the effective charge transport and, as a consequence, enhance recombination losses. The low FF could be explained by a strong dependence of the charge photogeneration efficiency on the electric field as the current density does not saturate at the negative voltages (Figure 7a). The J_{SC} values for all compounds are in full accordance with the maximum EQE values. The J_{SC} values calculated from the EQE spectra are in good agreement with the J_{SC} value obtained from the J - V curves. The highest J_{SC} values for **TPA**, **m-TPA** and **BTI** also correspond to the most red-shifted EQE spectra (Figure 7c).

2.4.2. Bulk-Heterojunction Solar Cells

Figure 8 compares J - V curves and EQE spectra of bulk-heterojunction solar cells based on blends with PC₇₁BM, and their photovoltaic properties are summarized in Table 6 (averaged photovoltaic parameters are presented in SI, Table S2). For a correct comparison we fabricated solar cells based on all blends with donor:acceptor mass ratio of 1:2 (as the optimal mass ratio for **TPA**:PC₇₁BM and **BTI**:PC₇₁BM was found to be 1:2 [56]). By using thermal annealing for the blends based on **f-TPA**, **t-CBZ** and **BTI**, which are able to crystallize according to the DSC data, we managed to slightly increase PCE within 10%. Note that solvent vapor annealing (o-dichlorobenzene) did not result in an increased PCE.

AFM study for BHJ solar cells was also carried out (SI, Figure S3.20). Similar to pristine films, a blended film based on **BTI** had a significantly different morphology and the highest RMS roughness of 1.28 nm, while the other blended films had similar smooth surfaces with a roughness in the range of 0.30–0.36 nm. Thus, it can be assumed that **BTI**:PC₇₁BM film is partially crystalline and differences in morphology of other films are present in the bulk.

As in the case of SC OSCs, BHJ solar cells based on **BTI** showed the highest efficiency, which may be due to the partial crystallinity of the active layer in accordance with AFM data (Figure S3.20f). **TPA**-based BHJ solar cells also had sufficiently high PCE. **f-TPA**-based BHJ solar cells had practically the same high efficiency, in contrast to the **f-TPA**-based SC OSC with the lowest PCE. **CBZ**-based BHJ solar cells had relatively low PCE values, as in the case of SC OSCs.

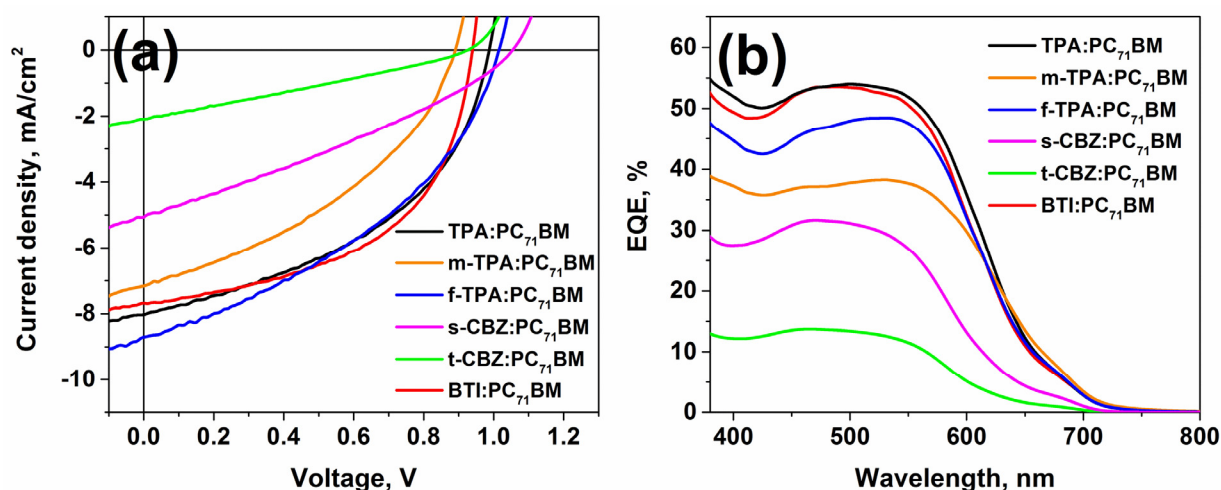


Figure 8. J - V curves under AM1.5G illumination (100 mW/cm^2) (a) and EQE spectra (b) for BHJ solar cells.

Table 6. The best photovoltaic parameters of BHJ solar cells under AM1.5G illumination (100 mW/cm^2), maximum EQE values.

Active Layer Material	J_{SC} , mA/cm^2	$J_{SC \text{ EQE}}^a$, mA/cm^2	V_{OC} , V	FF, %	PCE, %	EQE, %
TPA:PC ₇₁ BM	8.03	7.68	0.99	45.1	3.59	54.7
m-TPA:PC ₇₁ BM	7.16	5.84	0.89	39.2	2.50	38.8
f-TPA:PC ₇₁ BM ^b	8.70	6.85	1.02	39.7	3.52	48.5
s-CBZ:PC ₇₁ BM	5.07	3.81	1.05	31.0	1.65	31.6
t-CBZ:PC ₇₁ BM ^b	2.09	1.62	0.93	27.8	0.54	13.8
BTI:PC ₇₁ BM ^b	7.67	7.42	0.94	52.9	3.81	53.6

Note: ^a $J_{SC \text{ EQE}}$ —short-circuit current integrated from the EQE spectrum. ^b Data for the annealed (70°C for f-TPA, 100°C for t-CBZ, 80°C for BTI) active layer.

BHJ solar cells differ mainly in J_{SC} , EQE and FF. The values of V_{OC} \sim 0.95–1.05 V are about the same (except for m-TPA). These small differences in V_{OC} correspond to identical differences in HOMO energies within 0.1 eV. The lowest V_{OC} of m-TPA-based solar cells in agreement with the highest HOMO energy for m-TPA.

To understand the reasons for the differences in J_{SC} , EQE and FF of BHJ solar cells, we measured the hole mobilities in the blended films (Figures S3.13–3.18, Table 7). We suggest that the electron mobilities are similar in all blends, as they are determined mainly by PC₇₁BM. The blended films based on TPA, m-TPA and BTI had the highest hole mobilities, which is in agreement with hole transport in the pristine films (Table 4). This explains the highest PCE for TPA and BTI. CBZ-based blends had relatively low hole mobilities and so the corresponding BHJ solar cells had the lowest efficiencies.

Table 7. Hole mobilities in the blended films.

Material	μ_h , cm^2/Vs
TPA:PC ₇₁ BM	$(9.8 \pm 1.1) \cdot 10^{-4}$
m-TPA:PC ₇₁ BM	$(1.4 \pm 0.3) \cdot 10^{-3}$
f-TPA:PC ₇₁ BM	$(9.6 \pm 1.7) \cdot 10^{-5}$
s-CBZ:PC ₇₁ BM	$(5.1 \pm 1.0) \cdot 10^{-4}$
t-CBZ:PC ₇₁ BM	$(4.5 \pm 0.7) \cdot 10^{-4}$
BTI:PC ₇₁ BM	$(6.1 \pm 1.1) \cdot 10^{-4}$

3. Conclusions

In summary, novel D–A star-shaped molecules m-TPA and f-TPA were synthesized. Investigation of their properties in comparison with the previously published analogs (s-CBZ, t-CBZ, BTI, TPA) made it possible to reveal the impact of the core type on the

structure–properties relationship for this series of star-shaped molecules. Varying the type of electron-donor core allows us to control the solubility, thermal, optical, electrochemical properties and photoelectric characteristics of SC and BHJ OSCs. The molecules that have a more rigid and planar core such as **t-CBZ**, **f-TPA** and **BTI** are able to crystallize as compared to the amorphous **s-CBZ**, **TPA**, **m-TPA**. The introduction of either methoxy or *p*-tolylmethene substituents into the **TPA** core leads to an increase in solubility compared to the pristine **TPA**. There is no unambiguous influence of the star-shaped molecule core type on the photovoltaic properties. In BHJ OSCs, the new molecule **f-TPA** is among the most efficient, but at the same time in SC OSCs **f-TPA** is the least efficient. For both types of OSCs, **BTI** and **TPA** have shown the best efficiencies. Thus, the results obtained demonstrate that the **BTI** and **TPA** cores are attractive building blocks to design promising small molecules for SC and BHJ OSCs.

Supplementary Materials: The following are available online at <https://www.mdpi.com/article/10.3390/en14123596/s1>, Figure S2.1: ^1H NMR spectrum of compound **3a** in Acetone- d_6 , Figure S2.2: ^{13}C NMR spectrum of compound **3a** in Acetone- d_6 , Figure S2.3: ^1H NMR spectrum of compound **3b** in Acetone- d_6 , Figure S2.4: ^{13}C NMR spectrum of compound **3b** in Acetone- d_6 , Figure S2.5: ^1H NMR spectrum of compound **4a** in CDCl_3 , Figure S2.6: ^{13}C NMR spectrum of compound **4a** in CDCl_3 , Figure S2.7: ^1H NMR spectrum of compound **4b** in CDCl_3 , Figure S2.8: ^1H NMR spectrum of compound **m-TPA** in CDCl_3 , Figure S2.9: ^{13}C NMR spectrum of compound **m-TPA** in CDCl_3 , Figure S2.10: ^1H NMR spectrum of compound **f-TPA** in CDCl_3 , Figure S2.11: ^{13}C NMR spectrum of compound **f-TPA** in CDCl_3 , Figure S3.1: *J-V* characteristics of **TPA** hole only devices, Figure S3.2: *J-V* characteristics of **m-TPA** hole only devices, Figure S3.3: *J-V* characteristics of **f-TPA** hole only devices, Figure S3.4: *J-V* characteristics of **s-CBZ** hole only devices, Figure S3.5: *J-V* characteristics of **t-CBZ** hole only devices, Figure S3.6: *J-V* characteristics of **BTI** hole only devices, Figure S3.7: *J-V* characteristics of **TPA** electron only devices, Figure S3.8: *J-V* characteristics of **m-TPA** electron only devices, Figure S3.9: *J-V* characteristics of **f-TPA** electron only devices, Figure S3.10: *J-V* characteristics of **s-CBZ** electron only devices, Figure S3.11: *J-V* characteristics of **t-CBZ** electron only devices, Figure S3.12: *J-V* characteristics of **BTI** electron only devices, Figure S3.13: *J-V* characteristics of **TPA:PC71BM** hole only devices, Figure S3.14: *J-V* characteristics of **m-TPA:PC71BM** hole only devices, Figure S3.15: *J-V* characteristics of **f-TPA:PC71BM** hole only devices, Figure S3.16: *J-V* characteristics of **s-CBZ:PC71BM** hole only devices, Figure S3.17: *J-V* characteristics of **t-CBZ:PC71BM** hole only devices, Figure S3.18: *J-V* characteristics of **BTI:PC71BM** hole only devices, Figure S3.19: AFM surface scans of films of **TPA**, RMS = 0.33 nm (a); **m-TPA**, RMS = 0.31 nm (b); **f-TPA**, RMS = 0.30 nm (c); **s-CBZ**, RMS = 0.36 nm (d); **t-CBZ**, RMS = 0.37 nm (e); **BTI**, RMS = 4.60 nm (f), Figure S3.20: AFM surface scans of films of **TPA:PC71BM**, RMS = 0.36 nm (a); **m-TPA:PC71BM**, RMS = 0.30 nm (b); **f-TPA:PC71BM**, RMS = 0.31 nm (c); **s-CBZ:PC71BM**, RMS = 0.33 nm (d); **t-CBZ:PC71BM**, RMS = 0.36 nm (e); **BTI:PC71BM**, RMS = 1.28 nm (f), Table S1: Photovoltaic parameters of SCOSCs under AM1.5G illumination (100 mW/cm²) averaged over eight devices, Table S2: Photovoltaic parameters of BHJ solar cells under AM1.5G illumination (100 mW/cm²) averaged over eight devices.

Author Contributions: Conceptualization, Y.N.L., D.Y.P., S.A.P.; Writing—Original Draft Preparation, A.N.S., Y.N.L.; Writing—Review and Editing, A.N.S., Y.N.L., A.L.M., A.V.B., M.A.S., S.N.C., D.Y.P., S.A.P.; Resources, A.N.S., Y.N.L.; Investigation, P.S.S., A.L.M., A.V.B.; Visualization, M.A.S.; Project Administration, Y.N.L. All authors have read and agreed to the published version of the manuscript.

Funding: The work was financially supported by Russian Science Foundation (grant number 19–73–10198) and carried out in ISPM RAS.

Institutional Review Board Statement: Not applicable.

Informed Consent Statement: Not applicable.

Data Availability Statement: Not applicable.

Acknowledgments: NMR and UV–vis spectra were recorded using the equipment of Collaborative Access Center ‘Center for Polymer Research’ of Enikolopov Institute of Synthetic Polymeric Materials of the Russian Academy of Sciences with the financial support from the Ministry of Science and Higher Education of the Russian Federation (Contract 0071-2019-0006). Authors acknowledge D.O.

Balakirev for providing BTI material for X-ray investigation. The work on solar cells was done using the equipment purchased under the Lomonosov Moscow State University Program of Development.

Conflicts of Interest: The authors declare no conflict of interest.

References

1. Li, Y.; Xu, G.; Cui, C.; Li, Y. Flexible and semitransparent organic solar cells. *Adv. Energy Mater.* **2018**, *8*, 1701791. [[CrossRef](#)]
2. Wang, G.; Adil, M.A.; Zhang, J.; Wei, Z. Large-area organic solar cells: Material requirements, modular designs, and printing methods. *Adv. Mater.* **2019**, *31*, e1805089. [[CrossRef](#)] [[PubMed](#)]
3. Ganesan, S.; Mehta, S.; Gupta, D. Fully printed organic solar cells—A review of techniques, challenges and their solutions. *Opto-Electron. Rev.* **2019**, *27*, 298–320. [[CrossRef](#)]
4. Wienhold, K.S.; Chen, W.; Yin, S.; Guo, R.; Schwartzkopf, M.; Roth, S.V.; Müller-Buschbaum, P. Following in operando the structure evolution-induced degradation in printed organic solar cells with nonfullerene small molecule acceptor. *Sol. RRL* **2020**, *4*, 2000251. [[CrossRef](#)]
5. Kuznetsov, P.M.; Proshin, P.I.; Nikitenko, S.L.; Lolaeva, A.V.; Vasil'Ev, S.G.; Troshin, P.A.; Akkuratov, A.V. Design of novel thiazolothiazole-based conjugated polymer for efficient fullerene and non-fullerene organic solar cells. *Synth. Met.* **2020**, *268*, 116508. [[CrossRef](#)]
6. Wienhold, K.S.; Körstgens, V.; Grott, S.; Jiang, X.; Schwartzkopf, M.; Roth, S.V.; Müller-Buschbaum, P. Effect of solvent additives on the morphology and device performance of printed nonfullerene acceptor based organic solar cells. *ACS Appl. Mater. Interfaces* **2019**, *11*, 42313–42321. [[CrossRef](#)]
7. Cui, Y.; Yao, H.; Zhang, J.; Zhang, T.; Wang, Y.; Hong, L.; Xian, K.; Xu, B.; Zhang, S.; Peng, J.; et al. Over 16% efficiency organic photovoltaic cells enabled by a chlorinated acceptor with increased open-circuit voltages. *Nat. Commun.* **2019**, *10*, 2515. [[CrossRef](#)]
8. Meng, L.; Zhang, Y.; Wan, X.; Li, C.; Zhang, X.; Wang, Y.; Ke, X.; Xiao, Z.; Ding, L.; Xia, R.; et al. Organic and solution-processed tandem solar cells with 17.3% efficiency. *Science* **2018**, *361*, 1094–1098. [[CrossRef](#)] [[PubMed](#)]
9. Xu, X.; Feng, K.; Bi, Z.; Ma, W.; Zhang, G.; Peng, Q. Single-Junction Polymer Solar Cells with 16.35% Efficiency Enabled by a Platinum(II) Complexation Strategy. *Adv. Mater.* **2019**, *31*, e1901872. [[CrossRef](#)]
10. Meier, H. Conjugated oligomers with terminal donor–Acceptor substitution. *Angew. Chem. Int. Ed.* **2005**, *44*, 2482–2506. [[CrossRef](#)]
11. Roncali, J.; Leriche, P.; Blanchard, P. Molecular materials for organic photovoltaics: Small is beautiful. *Adv. Mater.* **2014**, *26*, 3821–3838. [[CrossRef](#)]
12. Schulze, K.; Uhrich, C.; Schüppel, R.; Leo, K.; Pfeiffer, M.; Brier, E.; Reinold, E.; Bäuerle, P. Efficient vacuum-deposited organic solar cells based on a new low-bandgap oligothiophene and fullerene C60. *Adv. Mater.* **2006**, *18*, 2872–2875. [[CrossRef](#)]
13. Patrizi, B.; Cozza, C.; Pietropaolo, A.; Foggi, P.; De Cumis, M.S. Synergistic approach of ultrafast spectroscopy and molecular simulations in the characterization of intramolecular charge transfer in push-pull molecules. *Molecules* **2020**, *25*, 430. [[CrossRef](#)] [[PubMed](#)]
14. Bureš, F. Fundamental aspects of property tuning in push-pull molecules. *RSC Adv.* **2014**, *4*, 58826–58851. [[CrossRef](#)]
15. Ledwon, P. Recent advances of donor-acceptor type carbazole-based molecules for light emitting applications. *Org. Electron.* **2019**, *75*, 105422. [[CrossRef](#)]
16. Feng, H.-T.; Zeng, J.; Yin, P.-A.; Wang, X.-D.; Peng, Q.; Zhao, Z.; Lam, J.W.Y.; Tang, B.Z. Tuning molecular emission of organic emitters from fluorescence to phosphorescence through push-pull electronic effects. *Nat. Commun.* **2020**, *11*, 2617. [[CrossRef](#)]
17. Roncali, J.; Leriche, P.; Cravino, A. From one- to three-dimensional organic semiconductors: In search of the organic silicon? *Adv. Mater.* **2007**, *19*, 2045–2060. [[CrossRef](#)]
18. Ripaud, E.; Olivier, Y.; Leriche, P.; Cornil, J.; Roncali, J. Polarizability and internal charge transfer in thiophene–triphenylamine hybrid π -conjugated systems. *J. Phys. Chem. B* **2011**, *115*, 9379–9386. [[CrossRef](#)]
19. Wu, H.-C.; Zhang, J.; Bo, Z.; Chen, W.-C. Well-defined star-shaped donor–acceptor conjugated molecules for organic resistive memory devices. *Chem. Commun.* **2015**, *51*, 14179–14182. [[CrossRef](#)]
20. Solodukhin, A.N.; Luponosov, Y.; Mannanov, A.; Dmitryakov, P.V.; Peregudova, S.M.; Chvalun, S.N.; Parashchuk, D.Y.; Ponomarenko, S.A. Effect of branching on the physical and photovoltaic properties of donor–acceptor oligomers based on triphenylamine. *Mendeleev Commun.* **2019**, *29*, 385–387. [[CrossRef](#)]
21. Popli, C.; Jang, Y.; Patil, Y.; Misra, R.; D'Souza, F. Formation of highly efficient, long-lived charge separated states in star-shaped ferrocene-diketopyrrolopyrrole-triphenylamine donor–acceptor–donor conjugates. *Chem. A Eur. J.* **2020**, *26*, 15109–15115. [[CrossRef](#)] [[PubMed](#)]
22. Kanibolotsky, A.L.; Perepichka, I.; Skabara, P.J. Star-shaped π -conjugated oligomers and their applications in organic electronics and photonics. *Chem. Soc. Rev.* **2010**, *39*, 2695–2728. [[CrossRef](#)]
23. Jarosz, T.; Lapkowski, M.; Ledwon, P. Advances in star-shaped π -conjugated systems: Properties and applications. *Macromol. Rapid Commun.* **2014**, *35*, 1006–1032. [[CrossRef](#)]
24. Lin, K.; Wang, S.; Wang, Z.; Yin, Q.; Liu, X.; Jia, J.; Jia, X.; Luo, P.; Jiang, X.; Duan, C.; et al. Electron acceptors with a truxene core and perylene diimide branches for organic solar cells: The effect of ring-fusion. *Front. Chem.* **2018**, *6*. [[CrossRef](#)] [[PubMed](#)]
25. Pan, Y.; Sun, G. Star-shaped non-fullerene small acceptors for organic solar cells. *ChemSusChem* **2019**, *12*, 4570–4600. [[CrossRef](#)] [[PubMed](#)]

26. Zhao, G.; Wu, G.; He, C.; Bai, F.-Q.; Xi, H.; Zhang, H.-X.; Li, Y. Solution-processable multiarmed organic molecules containing triphenylamine and DCM Moieties: Synthesis and photovoltaic properties. *J. Phys. Chem. C* **2009**, *113*, 2636–2642. [[CrossRef](#)]
27. Singh, S.P.; Roy, M.S.; Thomas, K.R.J.; Balaiah, S.; Bhanuprakash, K.; Sharma, G.D. New triphenylamine-based organic dyes with different numbers of anchoring groups for dye-sensitized solar cells. *J. Phys. Chem. C* **2012**, *116*, 5941–5950. [[CrossRef](#)]
28. Metri, N.; Sallenave, X.; Plesse, C.; Beouch, L.; Aubert, P.-H.; Goubard, F.; Chevrot, C.; Sini, G. Processable star-shaped molecules with triphenylamine core as hole-transporting materials: Experimental and theoretical approach. *J. Phys. Chem. C* **2012**, *116*, 3765–3772. [[CrossRef](#)]
29. Luponosov, Y.N.; Solodukhin, A.N.; Balakirev, D.O.; Surin, N.M.; Svidchenko, E.A.; Pisarev, S.; Fedorov, Y.V.; Ponomarenko, S.A. Triphenylamine-based luminophores with different side and central aromatic blocks: Synthesis, thermal, photophysical and photochemical properties. *Dye. Pigment.* **2020**, *56*, 104–134. [[CrossRef](#)]
30. Zhou, P.; Dang, D.; Wang, Q.; Duan, X.; Xiao, M.; Tao, Q.; Tan, H.; Yang, R.; Zhu, W. Enhancing the photovoltaic performance of triphenylamine based star-shaped molecules by tuning the moiety sequence of their arms in organic solar cells. *J. Mater. Chem. A* **2015**, *3*, 13568–13576. [[CrossRef](#)]
31. Lian, X.; Zhao, Z.; Cheng, D. Recent progress on triphenylamine materials: Synthesis, properties, and applications. *Mol. Cryst. Liq. Cryst.* **2017**, *648*, 223–235. [[CrossRef](#)]
32. Cabanetos, C.; Blanchard, P.; Roncali, J. Arylamine based photoactive push-pull molecular systems: A brief overview of the chemistry “Made in Angers”. *Chem. Rec.* **2019**, *19*, 1123–1130. [[CrossRef](#)]
33. Luponosov, Y.N.; Min, J.; Solodukhin, A.N.; Kozlov, O.V.; Obrezkova, M.A.; Peregodova, S.M.; Ameri, T.; Chvalun, S.N.; Pshenichnikov, M.S.; Brabec, C.J.; et al. Effects of electron-withdrawing group and electron-donating core combinations on physical properties and photovoltaic performance in D- π -A star-shaped small molecules. *Org. Electron.* **2016**, *32*, 157–168. [[CrossRef](#)]
34. Huang, B.; Yin, Z.; Ban, X.; Ma, Z.; Jiang, W.; Tian, W.; Yang, M.; Ye, S.; Lin, B.; Sun, Y. Nondoped deep blue OLEDs based on Bis-(4-benzenesulfonyl-phenyl)-9-phenyl-9 H -carbazoles. *J. Lumin.* **2016**, *172*, 7–13. [[CrossRef](#)]
35. Bakirov, A.V.; Solodukhin, A.N.; Luponosov, Y.N.; Svidchenko, E.A.; Obrezkova, M.A.; Peregodova, S.M.; Shcherbina, M.A.; Ponomarenko, S.A.; Chvalun, S.N. The effect of star-shaped oligothiophenes with a carbazole core on their structural and optical properties. *Nanotechnol. Russ.* **2017**, *12*, 385–394. [[CrossRef](#)]
36. Dong, Q.; Lian, H.; Gao, Z.; Guo, Z.; Xiang, N.; Zhong, Z.; Guo, H.; Huang, J.; Wong, W.-Y. Novel spirofluorene/indole/carbazole-based hole transport materials with high triplet energy for efficient green phosphorescent organic light-emitting diodes. *Dye. Pigment.* **2017**, *137*, 84–90. [[CrossRef](#)]
37. Grybauskaitė-Kaminskiene, G.; Volyniuk, D.; Mimaite, V.; Bezvikonny, O.; Buciskas, A.; Bagdziunas, G.; Grazulevicius, J.V. Aggregation-enhanced emission and thermally activated delayed fluorescence of derivatives of 9-phenyl-9h -carbazole: Effects of methoxy and tert -butyl substituents. *Chem. A Eur. J.* **2018**, *24*, 9581–9591. [[CrossRef](#)]
38. Paek, S.; Cho, N.; Cho, S.; Lee, J.K.; Ko, J. Planar star-shaped organic semiconductor with fused triphenylamine core for solution-processed small-molecule organic solar cells and field-effect transistors. *Org. Lett.* **2012**, *14*, 6326–6329. [[CrossRef](#)]
39. Jiang, Z.-Q.; Chen, Y.; Yang, C.; Cao, Y.; Tao, Y.; Qin, J.; Ma, D. A fully diarylmethylene-bridged triphenylamine derivative as novel host for highly efficient green phosphorescent OLEDs. *Org. Lett.* **2009**, *11*, 1503–1506. [[CrossRef](#)] [[PubMed](#)]
40. Jiang, Z.; Ye, T.; Yang, C.; Yang, D.; Zhu, M.; Zhong, C.; Qin, J.; Ma, D. Star-shaped oligotriarylamines with planarized triphenylamine core: Solution-processable, high-tg-hole-injecting and hole-transporting materials for organic light-emitting devices. *Chem. Mater.* **2011**, *23*, 771–777. [[CrossRef](#)]
41. Robertson, N.; Parsons, S.; MacLean, E.J.; Coxall, R.A.; Mount, A.R. Preparation, X-ray structure and properties of a hexabrominated, symmetric indole trimer and its TCNQ adduct: A new route to functional molecular systems. *J. Mater. Chem.* **2000**, *10*, 2043–2047. [[CrossRef](#)]
42. Shao, J.; Guan, Z.; Yan, Y.; Jiao, C.; Xu, Q.-H.; Chi, C. Synthesis and characterizations of star-shaped octupolar triazatruxenes-based two-photon absorption chromophores. *J. Org. Chem.* **2011**, *76*, 780–790. [[CrossRef](#)]
43. Connell, A.; Wang, Z.; Lin, Y.-H.; Greenwood, P.C.; Wiles, A.A.; Jones, E.W.; Furnell, L.; Anthony, R.; Kershaw, C.P.; Cooke, G.; et al. Low cost triazatruxene hole transporting material for >20% efficiency perovskite solar cells. *J. Mater. Chem. C* **2018**, *7*, 5235–5243. [[CrossRef](#)]
44. Rakstys, K.; Abate, A.; Dar, M.I.; Gao, P.; Jankauskas, V.; Jacopin, G.; Kamarauskas, E.; Kazim, S.; Ahmad, S.; Grätzel, M.; et al. Triazatruxene-based hole transporting materials for highly efficient perovskite solar cells. *J. Am. Chem. Soc.* **2015**, *137*, 16172–16178. [[CrossRef](#)]
45. Li, X.-C.; Wang, C.-Y.; Lai, W.-Y.; Huang, W. Triazatruxene-based materials for organic electronics and optoelectronics. *J. Mater. Chem. C* **2016**, *4*, 10574–10587. [[CrossRef](#)]
46. Cravino, A.; Leriche, P.; Aleveque, O.; Roquet, S.; Roncali, J. Light-emitting organic solar cells based on a 3d conjugated system with internal charge transfer. *Adv. Mater.* **2006**, *18*, 3033–3037. [[CrossRef](#)]
47. Roncali, J. Single material solar cells: The next frontier for organic photovoltaics? *Adv. Energy Mater.* **2011**, *1*, 147–160. [[CrossRef](#)]
48. Yu, P.; Feng, G.; Li, J.; Li, C.; Xu, Y.; Xiao, C.; Li, W. A selenophene substituted double-cable conjugated polymer enables efficient single-component organic solar cells. *J. Mater. Chem. C* **2020**, *8*, 2790–2797. [[CrossRef](#)]

49. Jiang, X.; Yang, J.; Karuthedath, S.; Li, J.; Lai, W.; Li, C.; Xiao, C.; Ye, L.; Ma, Z.; Tang, Z.; et al. Miscibility-controlled phase separation in double-cable conjugated polymers for single-component organic solar cells with efficiencies over 8%. *Angew. Chem.* **2020**, *132*, 21867–21876. [[CrossRef](#)]
50. Marinelli, M.; Lanzi, M.; Liscio, A.; Zaneli, A.; Zangoli, M.; Di Maria, F.; Salatelli, E. Single-material organic solar cells with fully conjugated electron-donor alkoxy-substituted bithiophene units and electron-acceptor benzothiadiazole moieties alternating in the main chain. *J. Mater. Chem. C* **2020**, *8*, 4124–4132. [[CrossRef](#)]
51. Nakayama, K.-I.; Okura, T.; Okuda, Y.; Matsui, J.; Masuhara, A.; Yoshida, T.; White, M.; Yumusak, C.; Stadler, P.; Scharber, M.; et al. Single-component organic solar cells based on intramolecular charge transfer photoabsorption. *Materials* **2021**, *14*, 1200. [[CrossRef](#)]
52. Dong, Y.; Nikolis, V.C.; Talnack, F.; Chin, Y.-C.; Benduhn, J.; Londi, G.; Kublitski, J.; Zheng, X.; Mannsfeld, S.C.B.; Spoltore, D.; et al. Orientation dependent molecular electrostatics drives efficient charge generation in homojunction organic solar cells. *Nat. Commun.* **2020**, *11*, 4617. [[CrossRef](#)] [[PubMed](#)]
53. Mannanov, A.L.; Savchenko, P.S.; Luponosov, Y.N.; Solodukhin, A.N.; Ponomarenko, S.A.; Paraschuk, D.Y. Charge photogeneration and recombination in single-material organic solar cells and photodetectors based on conjugated star-shaped donor-acceptor oligomers. *Org. Electron.* **2020**, *78*, 105588. [[CrossRef](#)]
54. Solodukhin, A.N.; Luponosov, Y.N.; Mannanov, A.L.; Paraschuk, D.Y.; Ponomarenko, S.A. Novel star-shaped donor-acceptor molecules based on trihenylamine for organic solar cells and photodetectors. In Proceedings of the Online School on Hybrid, Organic and Perovskite Photovoltaics, Moscow, Russia, 3–5 November 2020; p. 24.
55. Min, J.; Luponosov, Y.N.; Baran, D.; Chvalun, S.N.; Shcherbina, M.A.; Bakirov, A.V.; Dmitryakov, P.V.; Peregudova, S.M.; Kausch-Busies, N.; Ponomarenko, S.A.; et al. Effects of oligothiophene π -bridge length on physical and photovoltaic properties of star-shaped molecules for bulk heterojunction solar cells. *J. Mater. Chem. A* **2014**, *2*, 16135–16147. [[CrossRef](#)]
56. Balakirev, D.O.; Luponosov, Y.N.; Mannanov, A.; Savchenko, P.S.; Minenkov, Y.; Paraschuk, D.Y.; Ponomarenko, S.A. Star-shaped benzotriindole-based donor-acceptor molecules: Synthesis, properties and application in bulk heterojunction and single-material organic solar cells. *Dye. Pigment.* **2020**, *181*, 108523. [[CrossRef](#)]
57. Luponosov, Y.N.; Solodukhin, A.N.; Mannanov, A.; Savchenko, P.S.; Minenkov, Y.; Paraschuk, D.Y.; Ponomarenko, S.A. Effect of fused triphenylamine core in star-shaped donor- π -acceptor molecules on their physicochemical properties and performance in bulk heterojunction organic solar cells. *Dye. Pigment.* **2020**, *177*, 108260. [[CrossRef](#)]
58. Luponosov, Y.N.; Min, J.; Solodukhin, A.N.; Bakirov, A.V.; Dmitryakov, P.V.; Shcherbina, M.A.; Peregudova, S.M.; Cherkaev, G.V.; Chvalun, S.N.; Brabec, C.J.; et al. Star-shaped D- π -A oligothiophenes with a tris(2-methoxyphenyl)amine core and alkyldicyanovinyl groups: Synthesis and physical and photovoltaic properties. *J. Mater. Chem. C* **2016**, *4*, 7061–7076. [[CrossRef](#)]
59. Luponosov, Y.N.; Balakirev, D.O.; Dyadishchev, I.V.; Solodukhin, A.N.; Obrezkova, M.A.; Svidchenko, E.A.; Surin, N.M.; Ponomarenko, S.A. In search of efficient solubilizing groups for liquid and luminescent oligo(phenylene-thiophene) chromophores. *J. Mater. Chem. C* **2020**, *8*, 17074–17082. [[CrossRef](#)]
60. Ripaud, E.; Rousseau, T.; Leriche, P.; Roncali, J. Unsymmetrical triphenylamine-oligothiophene hybrid conjugated systems as donor materials for high-voltage solution-processed organic solar cells. *Adv. Energy Mater.* **2011**, *1*, 540–545. [[CrossRef](#)]
61. Kozlov, O.V.; Luponosov, Y.N.; Ponomarenko, S.A.; Kausch-Busies, N.; Paraschuk, D.Y.; Olivier, Y.; Beljonne, D.; Cornil, J.; Pshenichnikov, M.S. Ultrafast charge generation pathways in photovoltaic blends based on novel star-shaped conjugated molecules. *Adv. Energy Mater.* **2014**, *5*, 1401657. [[CrossRef](#)]
62. Roncali, J.; Grosu, I. The dawn of single material organic solar cells. *Adv. Sci.* **2019**, *6*, 1801026. [[CrossRef](#)] [[PubMed](#)]